Materialia 25 (2022) 101545

Contents lists available at ScienceDirect

Materialia

journal homepage: www.elsevier.com/locate/mtla

Full Length Article

Uncovering the deformation pathways of additive manufactured Ti-6Al-4V with engineered duplex microstructure

Jenniffer Bustillos [a,b], Atieh Moridi [a,*]

[a] Sibley School of Mechanical and Aerospace Engineering, Cornell University, 124 Hoy Road, 469 Upson Hall, Ithaca, NY 14853, USA
[b] Kavli Institute at Cornell for Nanoscale Science, 420 Physical Sciences Building, Ithaca, NY 14853, USA

ARTICLE INFO

Keywords:
Microstructure engineering
L-PBF
Titanium alloys
Additive manufacturing
Dislocation substructures

ABSTRACT

Directional thermal gradients, high cooling rates and stochastic powder-laser interactions during additive manufacturing (AM) result in printed Ti alloys with anisotropic properties, high strength but reduced ductility. Harnessing the inherent AM defects and using a standardized thermomechanical process, the authors designed a Ti alloy with duplex microstructure that overcomes the strength-ductility trade-off while reducing anisotropy. Here, we uncover the deformation mechanisms of the Ti-6Al-4V duplex microstructure consisting of defect-free globular α-grains and hierarchical α-laths. Evaluation of the tensile surface reveals that the deformation begins with the early saturation of work hardening in α-laths, followed by the emergence of interfacial back stress hardening, and finally the transfer of strains to globular α-grains. Plastic strains partaken by the globular α-grains prompt crystal rotations to "softer" orientations (basal, and prismatic) and generate a fine network of dislocation cells. These findings suggest the ability to push property limits of structural materials by microstructure engineering during AM.

Laser-powder bed fusion (L-PBF) is a rapidly maturing technique that has allowed the manufacturing of parts with complex geometries, high resolution and mechanical strength but typically reduced ductility [1,2]. Particularly for the $\alpha+\beta$ Ti alloy (Ti-6Al-4V), the rapid cooling rates and intrinsic cyclic heat treatment produce hierarchical microstructures of α'-martensite laths with residual strain and strong crystallographic texture [1,3–7]. As a result, L-PBF Ti-6Al-4V tends to exhibit tensile strengths of up to 1.2 GPa but low failure strains between 1.6–11.9% accentuating the strength-ductility trade-off [3–6,8].

Efforts to improve the ductility of printed Ti-6Al-4V include *in-situ* and post-processing treatments or a combination of both [6–16]. More commonly, L-PBF Ti-6Al-4V is post-processed via hot isostatic pressing (HIP) to stabilize phases, partially recover ductility and close defects [1,6–10]. However, standardized sub-transus HIP has a marginal effect on the ductility and work hardening due to the inability to modify the crystallographic, and morphological nature of the microstructure [10,17,18]. Guided by metallurgical principles [19–21], our group implemented a paradoxical strategy to engineer a duplex microstructure in L-PBF Ti-6Al-4V consisting of α-laths (prior α'-martensite) and recrystallized globular α-grains (Fig. 1 a, b) [18]. Harnessing the strength of α-laths and plasticity of globular α-grains, the duplex microstructure ($\varepsilon_f = 20 \pm 1\%$) outperforms the ductility of fully dense (FD) as-printed ($\varepsilon_f = 5 \pm 1\%$) and HIPed counterparts ($\varepsilon_f = 10 \pm 1\%$) (Fig. 1 c, d) [18]. Despite the potential showed by the engineered microstructure, the deformation mechanisms of the duplex microstructure remain unknown. In this study, we investigate mechanisms responsible for the extended plasticity ($\varepsilon_f = 20 \pm 1\%$) and retained strength (ultimate tensile strength (UTS) = 1.06 ± 0.02 GPa) of the Ti-6Al-4V with duplex microstructure, revealing heterogenous distribution of strains and dislocation cell evolution.

The Ti-6Al-4V with duplex microstructure was manufactured via L-PBF technique under LoF regime and HIPed with sub-transus temperatures (900 °C, 100 MPa, 120 min) (LoF-HIP) [18]. A control specimen using optimal printing conditions was manufactured, and HIPed following same post-processing conditions, representing a commonly employed procedure of L-PBF Ti parts (FD-HIP). Manufacturing and post-process parameters are detailed in the authors' earlier publication [18]. Tensile experiments were carried out on polished specimens using a Deben MT 2000 micro-tensile stage with a 2 kN load cell (Deben UK Ltd, Suffolk, UK) at a strain rate of $1.3 \times 10\text{-}3\ s^{-1}$. Tensile strains were captured via digital image correlation (DIC) (GOM, Braunschweig, Germany). Microstructure, texture, and grain orientation evolution were evaluated in a Tescan Mira field emission scanning electron microscope (FE-SEM) via electron backscatter diffraction (EBSD), using a QUANTAX EBSD (Bruker, Billerica, MA, USA) apparatus.

The tensile behavior of as-printed, FD-HIP and LoF-HIP specimens is shown in Fig. 1 e. The limited ductility in as-printed Ti-6Al-4V combined with a yield strength of 1095.4 ± 56.4 MPa and UTS of

* Corresponding author.
E-mail address: moridi@cornell.edu (A. Moridi).

https://doi.org/10.1016/j.mtla.2022.101545
Received 5 August 2022; Accepted 13 August 2022
Available online 14 August 2022

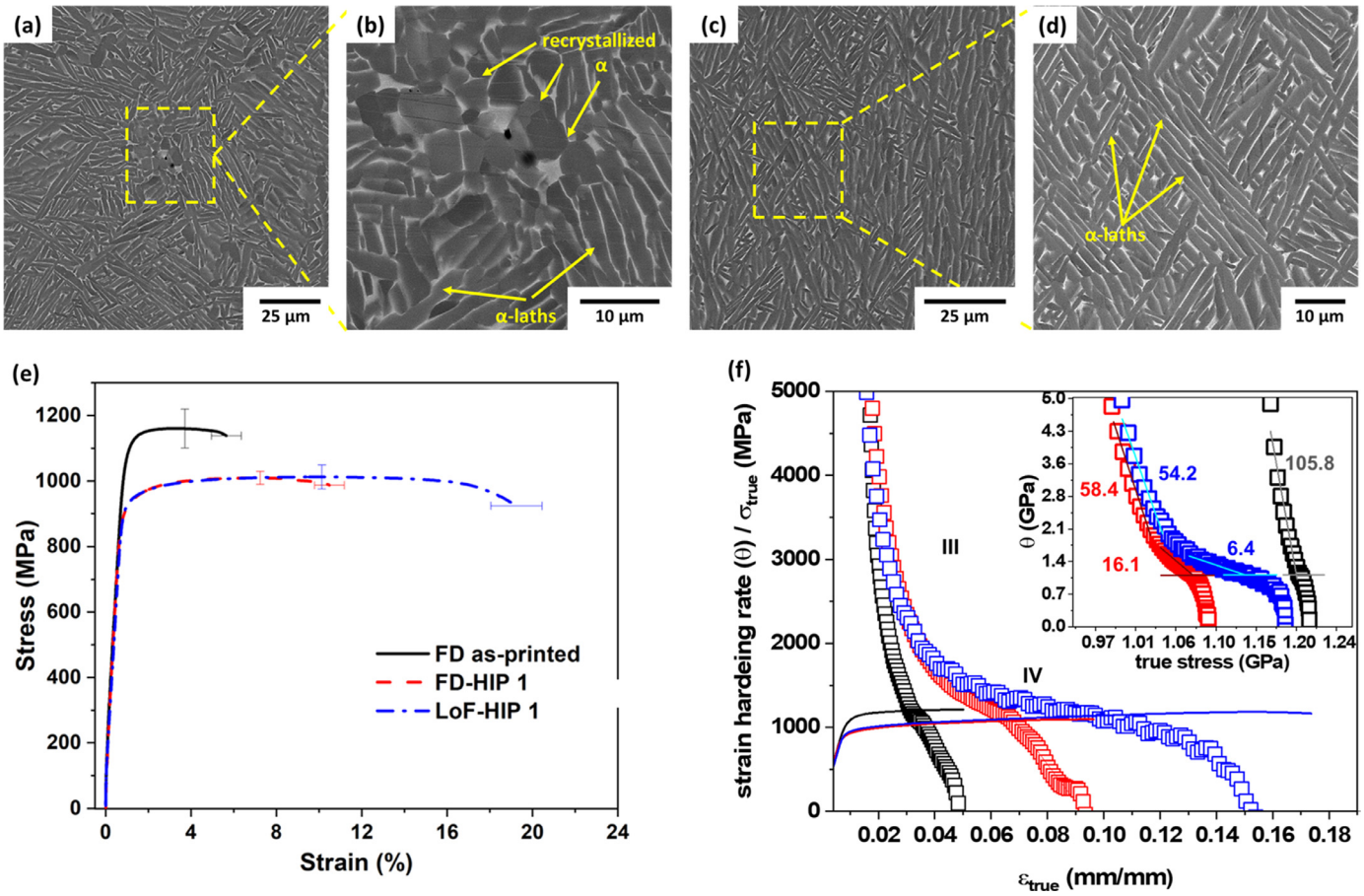

Fig. 1. Scanning electron micrographs showing the microstructure of undeformed (a, b) LoF-HIP speicmen with duplex microstructure, (c, d) FD-HIP specimen with a hierarchichal microstructures of α-laths. (e) Average tensile stress-strain curves and (f) strain hardening rate (Θ) curves as a function of true strain with superimposed true stress-true strain curves show the onset of necking as described by Considere criterion (σ=dσ/dε). Inset in (f) shows the Kocks-Mecking (K-M) curves of all specimens during plastic deformation.

$1.1 \pm 6 \times 10^{-2}$ GPa is attributed to the presence of a fully martensitic phase with residual thermal strain [4,18]. HIP results in a decrease of yield strength in FD samples to 945.9 ± 30 MPa and slight changes in the UTS to $1.01 \pm 2 \times 10^{-2}$ GPa. On the other hand, defect reduction and recrystallization in LoF-HIP combines a fracture strain of 20 ± 1%, a yield strength (925.5 ± 21 MPa) and UTS ($1.0 \pm 3 \times 10^{-2}$ GPa) comparable to FD-HIP.

It is inferred from the tensile and work hardening rate curves ($\theta = \delta\sigma_t/\delta\varepsilon_t$) (Fig. 1 e, f), that FD as-printed and FD-HIP have a short range of strain hardening prior to the necking onset ($n_{\text{as-printed}}$: $0.03 \pm 2.3 \times 10^{-4}$, $n_{\text{FD-HIP}}$: $0.07 \pm 1.2 \times 10^{-4}$). Whereas LoF-HIP shows a prolonged quasi-stable deformation regime prior to necking instabilities ($n_{\text{LoF-HIP}}$: $0.11 \pm 2.1 \times 10^{-4}$).

All specimens exhibit typical strain hardening (Θ) stages III and IV with distinct decreasing slopes (Fig. 1 f) [22–24]. First, a sharp drop in Θ of all specimens at ε_t=0.015–0.04 initiates stage III which is associated with the evolution of dislocation cells and dynamic recovery events [22,24,25]. This is followed by stage IV with a slope change up to the limit of instabilities (σ_{UTS}). Due to the decreased plasticity in FD as-printed, stage IV is short-lived and only stage III is apparent from Kocks-Mecking (K-M) curves (inset of Fig. 1 f) indicating the limited dislocation hardening capability of this material [22,24,25]. The K-M relationship is commonly described as $\Theta = \Theta_o - c_b \cdot \sigma$, where the available uniform plasticity depends on a softening factor, c_b [23–25]. Linear fitting of the K-M curves between σ_y and σ_{UTS} showcases FD as-printed to have a single c_b of 105.8 ± 1, while FD-HIP and LoF-HIP exhibit an initial c_b of 58.4 ± 0.5 and 54.2 ± 0.8 followed by a lower c_b in stage IV of 16.1 ± 0.1 and 6.4 ± 0.1, respectively. The computed values herein agree with reported literature and showcase the tendency of a decreasing c_b as a signal to increased uniform plasticity [24].

Work hardening in Ti-6Al-4V is largely attributed to the evolution and storage of dislocations at increasing strain, dislocation pile-up and substructure formation [26–28]. The rapid decrease of Θ in FD as-printed is caused by its inherent dislocation dense α'-lath microstructure limiting further dislocation activity and is reflected in its high c_b [29]. On the other hand, HIP results in the transformation of α' to equilibrium α+β and the reduction of dislocation density [1,6–10,30]. This leads to the restoration of the hardening capability as observed by the higher Θ in stage III and decrease in c_b by ~50% with respect to the FD as-printed samples.

As plastic deformation begins, defects, stress concentrations and grain boundaries act as sources for the emission of mobile dislocations that glide across favorable slip systems following the critical resolved shear stress (CRSS) [31,32]. In the case of FD-HIP, inherited microstructure morphology and pre-existing dislocation tangles reduce the mean free path for emerging dislocations preventing further work hardening [32]. The enhanced work-hardening and uniform elongation in LoF-HIP is attributed to the presence of dislocation-free α-grains among α-laths with prior thermal history making up the duplex microstructure [18,33–35]. These indicate that the inherited AM lattice defects and nature of grains affect the plastic limit of the L-PBF part even after a conventional sub-transus HIP schedule.

Given the heterogenous strain distribution experienced across the tensile surfaces (Fig. S1), a single specimen is able to provide a broad

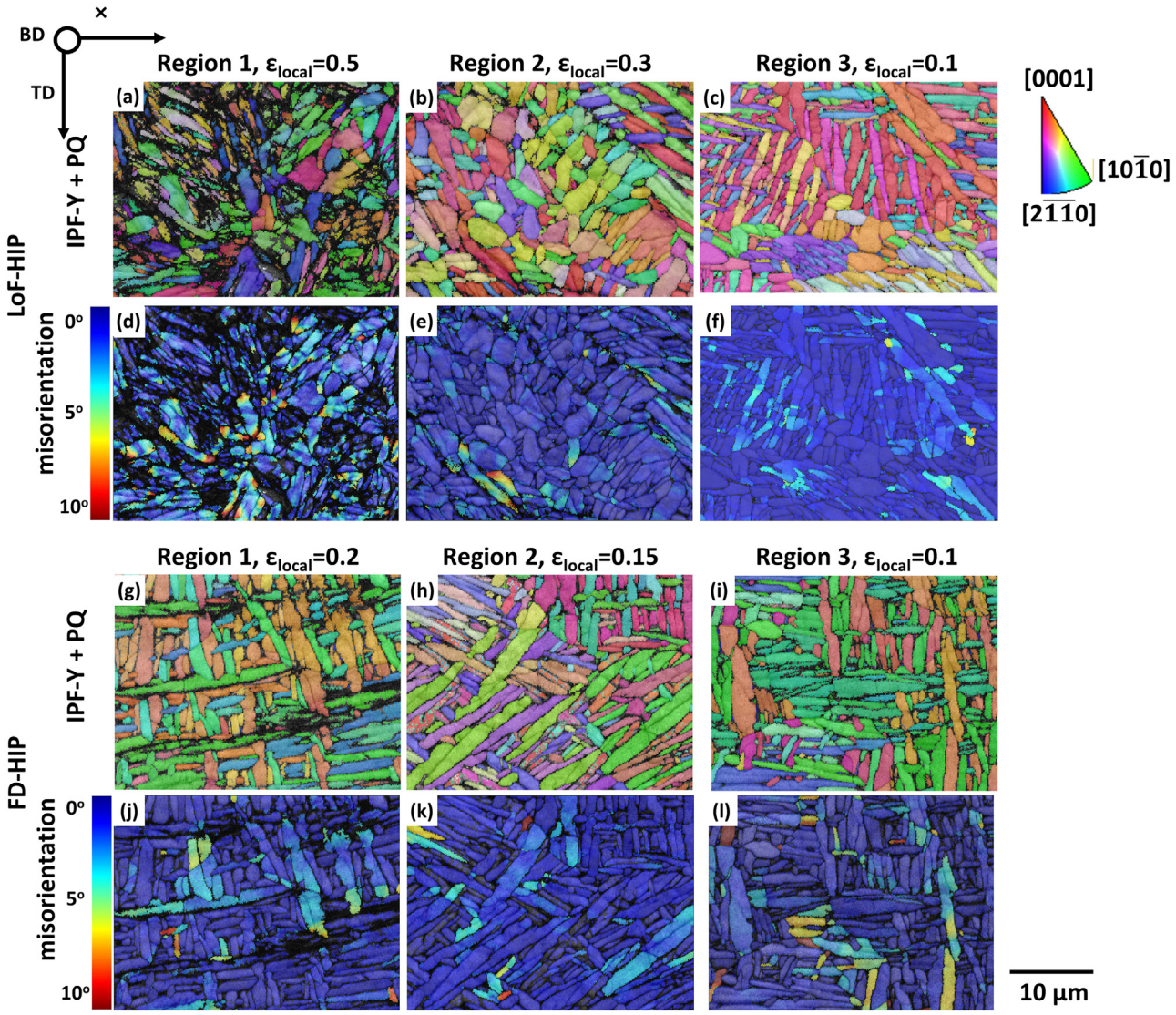

Fig. 2. Post-mortem inverse pole figure and pattern quality overlay maps taken parallel to the tensile direction for the α-phase in three distinct strain state regions of the (a–c) LoF-HIP, and (j–l) FD-HIP. Grain reference orientation deviation maps showing lattice rotations with reference to the average grain orientations of (d–f) LoF-HIP and (j–l) FD-HIP specimens.

range of strain levels detailing deformation evolution features. Post-mortem EBSD scans captured three regions along the tensile surface with areas of 34 × 26 μm^2 and step size of 0.09 μm to resolve grain substructures. The three regions of analysis correspond to region 1 (close to the fracture region), region 2 (0.4 mm from fracture), and region 3 (~3 mm from fracture). Fig. 2 a–c, f–h show the α-phase inverse pole figure (IPF) maps of LoF-HIP and FD-HIP, respectively. The direction of observation is aligned with the tensile direction (i.e., IPF-Y). As observed from the IPF, the microstructure of the LoF-HIP specimen consists of globular α-grains and hierarchical α-laths, while FD-HIP solely comprises of α-laths.

Analysis of the (0001) pole figures revealed the LoF-HIP specimen to experience a decrease in texture with increasing local strains shown by the multiples of random distribution (m.r.d.$_{\text{LoF-HIP}}$: 12–39) (Fig. S2). The texture components in regions 1, 2 and 3 correspond to grains with their c-axis at 71 °, 85 ° and 74.4° with respect to the (0001) pole (i.e., building direction), respectively. On the other hand, FD-HIP shows negligible changes in texture across the strained surface (m.r.d.$_{\text{FD-HIP}}$: 32–49). Texture components correspond to grains with their c-axis tilted at 34.5° and 60° away from the (0001) pole. It should be noted that region 3 in LoF-HIP shows a higher density of α-laths, hence, the grain morphology and texture is similar to that observed in FD-HIP (maximum m.r.d$_{\text{region3}}$: 39). The increased variation in crystal orientations in region 1 and 2 compared to 3 of LoF-HIP is attributed to the higher degree of grain rotation and slip activity to accommodate high local strains (Fig. S2 d–f).

Strong deformation zones can be distinguished in the region 1-IPF map of both specimens (Fig. 2 a, g) by the degradation of the EBSD pattern quality (PQ). In the case of the LoF-HIP specimen, the PQ degradation is larger and is associated with a higher defect density [36]. Regions 2 and 3 in FD-HIP see a uniform IPF map with minor signs of degraded PQ as a result of reduced local strains. At the grain scale, the intragranular orientation gradients observed reference to the accommodation of plastic deformation via lattice rotations [37,38] Lattice rotation as a function of tensile strains is evaluated via grain reference orientation deviation (GROD) analysis (Fig. 2 d–f, k–m). High misorientation spots indicate local dislocation density, pronounced lattice rotation, and/or presence of substructures. At low tensile strains ($\varepsilon_{\text{local}}$ = 0.07-0.1), lattice deformations produce misorientations of < 7°, with the maximum GROD observed at the tip of the α-laths in both HIP specimens (Fig. 2 f,

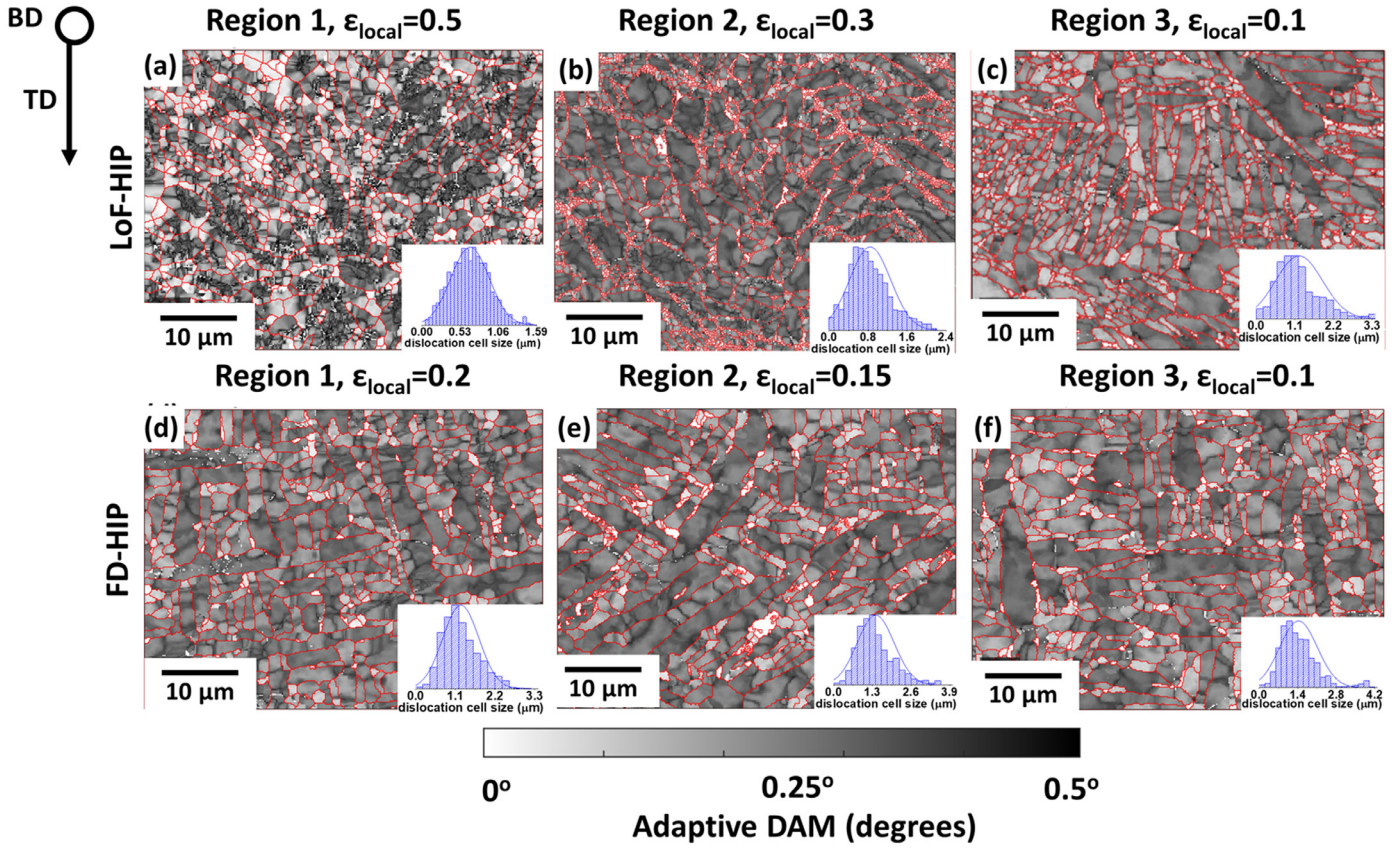

Fig. 3. Dense dislocation cell walls with $\Delta\theta = 0.5^{o}$ in (a–c) LoF-HIP and (d–f) FD-HIP specimens elucidated by adaptive domain misorientation approach analysis. Inset shows the frequency distribution of dislocation cell size with gaussian distributions.

l). Increase in strains to $\varepsilon_{local} = 0.3$ in LoF-HIP and $\varepsilon_{local} = 0.15$ in FD-HIP increase the maximum GROD to up to 10^{o} with the highest intragranular orientation gradients in primary α-laths with high aspect ratio [4]. These local deformation spots are reflected in Θ-stage III signaling to the initial easy slip in α-laths with crystallographic orientations suitable for strain localization [4]. An increase in local strains to $\varepsilon_{local} = 0.5$ prior to fracture in LoF-HIP shows maximum GROD sites (15^{o}) within globular α-grains (Fig. 2 d). These grains are also shown to exhibit high Schmidt factors >0.4 along basal and prismatic <a> type slips (Fig. S3a–c).This shift in preferential deformation site hints at the presence of a kinematic hardening effect in the duplex microstructure.

As for FD-HIP, local strain of $\varepsilon_{local} = 0.2$ in region 1 (Fig. 2 j) resulted in isolated spots of high GROD of up to 10^{o} within primary α-laths, showing the poor strain distribution to neighboring grains as a cause for premature fracture. It is noteworthy that these high GROD spots located at the tip of the α-laths form boundary junctions and intensify boundary interactions. Thus, despite primary α-laths inheriting easy slip orientations, their deformation is hindered by the limited slip transfer to accommodate further plastic strains in neighboring grains (Fig. S3d–f).

Employing an adaptive domain misorientation approach (DAM) in the analysis of conventional EBSD data, we reveal induced sub-grain and dislocation cell-wall features [37]. Informed by a convergence study, DAM analysis was performed using a kernel size of 16 μm (80 nearest neighbors (nn)). Fig. 3 shows the network of dislocation cells in LoF-HIP and FD-HIP. Dislocation cells emerge in response to the increased density of trapped dislocations rearranging to form walls, reducing the overall strain energy [37–40]. These substructures have low angle misorientations ($<1^{o}$) and act as effective barriers for further dislocation mobility [37,40]. DAM analysis in non-deformed specimens reveals an existing dislocation network in the LoF-HIP and FD-HIP specimens with average cell size of 1.03 ± 0.41 μm and 1.85 ± 0.9 μm, respectively. These defects result from the partial recovery of AM process induced dislocations, machining and/or sample preparation introduced strains. Further, a reduced dislocation cell size in LoF-HIP comes from the smaller average grain size compared to its counterpart and is beneficial to the strength of the alloy as described by Hall Petch's relationship [18,41]. In agreement with GROD analysis, there is a negligible change in the average dislocation cell size (LoF-HIP: 1.22 ± 0.7 μm, FD-HIP: 1.42 ± 0.7 μm) of both specimens at local strains of ε_{local} = 0.07-0.1 (region 3). At $\varepsilon_{local} = 0.3$ dislocation cells in LoF-HIP are refined to an average cell size of 0.89 ± 0.4 μm. Increase to $\varepsilon_{local} = 0.5$, promotes even further cell refinement to 0.67 ± 0.3 μm. These results confirm the high capacity to work harden high-stress regions in the LoF-HIP by evolving dislocation substructures. Quantitative analysis of region 1 and 2 in FD-HIP reveal negligible changes in the average dislocation cell size compared to region 3 (region $1_{FD\text{-}HIP}$ = 1.25 ± 0.5 μm, region $2_{FD\text{-}HIP}$ = 1.41 ± 0.6 μm). Thus, confirming the limited plasticity in a FD-HIP specimen results from the limited dislocation activity (i.e., cell formation and low angle boundary substructures). By asserting the average cell diameter of the substructures formed in region 1 of LoF-HIP and FD-HIP, we estimate the stress sustained prior to fracture as a measure of dislocation strengthening via Holt's relation [38–40]:

$$d = K\frac{1}{\sqrt{\rho}} \quad (1)$$

where, d is the average dislocation cell size, K is a material property constant, and ρ is the dislocation density. Taking the average cell size obtained via DAM analysis of region 1 in both specimens reveals that LoF-HIP sustains a dislocation density 3.5 times larger than that experienced by the FD-HIP. Further, the dislocation strengthening can be described via the classic Taylor relationship [40,42]:

$$\sigma = M\alpha G b\rho^{0.5} \quad (2)$$

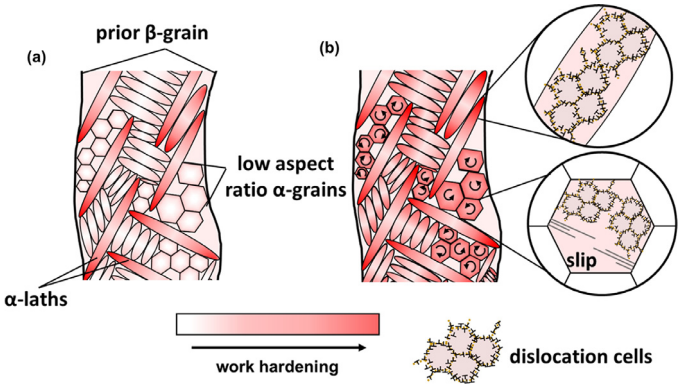

Fig. 4. Schematic representation of the deformation mechanisms in the Ti alloy with duplex microstructure (LoF-HIP): (a) Initial saturation of dislocation motion within primary α-lath's and (b) subsequent strain transfer to dislocation-free α-globules enabling extended work hardening and ductility via dislocation cell formation and rotation to "soft" crystallographic orientations suitable for slip.

where, M represents the Taylor factor, α is a dislocation interaction constant, G is the shear modulus, and b is the burgers vector taken as 0.29 nm (prismatic) and 0.306 nm (basal and pyramidal) [40,42]. Given that the material system remains constant, and assuming dislocation glide in both specimens occurs preferentially along prismatic and basal slip systems, the relative strengthening due to dislocations in LoF-HIP is up to ~2 times larger than that of FD-HIP.

It can be concluded that the deformation and strength of the duplex microstructure begins with the selective deformation of primary α-laths with soft configurations (Fig. 4 a), where dislocations are pinned at the grain boundary junctions. At this point, the increased dislocation densities will form dislocation substructures and saturate the work hardening of α-laths (Fig. 4 a) [38]. In the case of LoF-HIP, high strain gradients at interfacing α-laths and globules will result in the pile-up of geometrically necessary dislocations (GNDs) leading to an apparent back stress hardening effect [43]. A counteracting force in the α-globules and makes them appear stronger and delay their plastic instabilities. Soon after, dislocations are emitted into the α-globules further strains will lead to the evolution of a fine network of dislocations and rotation towards soft crystallographic orientations (Fig. S3 a–c) [43]. In the absence of the latter (FD-HIP), the energy required for dislocation climb/glide increases favoring fracture over slip activity.

The results herein, uncover strain hardening and back stress hardening as contributors to the plasticity in the engineered duplex microstructure of an AM Ti-6Al-4V. Local EBSD analysis confirms that an AM part printed using optimal parameters, and its subsequent HIP, results in a microstructure with limited work-hardenability and dislocation activity. In contrast, the synergistic effect of recrystallized α-grains and dislocation dense α-laths making up the duplex microstructure benefits from the effective strain transfer, lattice rotation to preferential slip orientations and excellent work hardenability.

Declaration of Competing Interest

The authors declare that they have no known competing financial interests or personal relationships that could have appeared to influence the work reported in this paper.

Acknowledgments

Authors acknowledge funding support by the Department of the Navy, Office of Naval Research. Young Investigator Award Number: N00014-22-1-2420. J.B. gratefully acknowledges funding received by the 2020-2021 Knight @ KIC Engineering Graduate Fellowship. The authors acknowledge Open Additive, LLC (Beavercreek, OH) and John Middendorf for the fabrication of SLM specimens used in this study. We also acknowledge Magnus Ahlfors at Quintus Technologies, LLC (Lewis Center, OH) for services provided in HIP post-processing of specimens. This work made use of the Cornell Center for Materials Research Shared Facilities which are supported through the NSF MRSEC program (DMR-1719875).

Supplementary materials

Supplementary material associated with this article can be found, in the online version, at doi:10.1016/j.mtla.2022.101545.

References

[1] S. Liu, Y.C. Shin, Additive manufacturing of Ti6Al4V alloy: A review, Mater. Des. 164 (2019) 107552, doi:10.1016/j.matdes.2018.107552.
[2] D. Gu, X. Shi, R. Poprawe, D.L. Bourell, R. Setchi, J. Zhu, Material-structure-performance integrated laser-metal additive manufacturing, Science 372 (2021) 1–15, doi:10.1126/science.abg1487.
[3] L. Parry, I.A. Ashcroft, R.D. Wildman, Understanding the effect of laser scan strategy on residual stress in selective laser melting through thermo-mechanical simulation, Addit. Manuf. 12 (2016) 1–15, doi:10.1016/j.addma.2016.05.014.
[4] A. Moridi, A.G. Demir, L. Caprio, A.J. Hart, B. Previtali, B.M. Colosimo, Deformation and failure mechanisms of Ti-6Al-4V as built by selective laser melting, Mater. Sci. Eng. A. 768 (2019) 138456, doi:10.1016/j.msea.2019.138456.
[5] B. Gorny, T. Niendorf, J. Lackmann, M. Thoene, T. Troester, H.J. Maier, In situ characterization of the deformation and failure behavior of non-stochastic porous structures processed by selective laser melting, Mater. Sci. Eng. A. 528 (2011) 7962–7967, doi:10.1016/j.msea.2011.07.026.
[6] C. Qiu, N.J.E. Adkins, M.M. Attallah, Microstructure and tensile properties of selectively laser-melted and of HIPed laser-melted Ti-6Al-4V, Mater. Sci. Eng. A. 578 (2013) 230–239, doi:10.1016/j.msea.2013.04.099.
[7] S. Leuders, M. Thöne, A. Riemer, T. Niendorf, T. Tröster, H.A. Richard, H.J. Maier, On the mechanical behaviour of titanium alloy TiAl6V4 manufactured by selective laser melting: Fatigue resistance and crack growth performance, Int. J. Fatigue. 48 (2013) 300–307, doi:10.1016/j.ijfatigue.2012.11.011.
[8] G. Kasperovich, J. Hausmann, Improvement of fatigue resistance and ductility of TiAl6V4 processed by selective laser melting, J. Mater. Process. Technol. 220 (2015) 202–214, doi:10.1016/j.jmatprotec.2015.01.025.
[9] M. Seifi, A. Salem, J. Beuth, O. Harrysson, J.J. Lewandowski, Overview of Materials Qualification Needs for Metal Additive Manufacturing, JOM 68 (2016) 747–764, doi:10.1007/s11837-015-1810-0.
[10] T. Vilaro, C. Colin, J.D. Bartout, As-fabricated and heat-treated microstructures of the Ti-6Al-4V alloy processed by selective laser melting, Metall. Mater. Trans. A Phys. Metall. Mater. Sci. 42 (2011) 3190–3199, doi:10.1007/s11661-011-0731-y.
[11] D.H. St John, S.D. McDonald, M.J. Bermingham, S. Mereddy, A. Prasad, M. Dargusch, The Challenges Associated with the Formation of Equiaxed Grains during Additive Manufacturing of Titanium Alloys, Key Eng. Mater. 770 (2018) 155–164 https://www.scientific.net/KEM.770.155.
[12] D. Zhang, D. Qiu, M.A. Gibson, Y. Zheng, H.L. Fraser, D.H. StJohn, M.A. Easton, Additive manufacturing of ultrafine-grained high-strength titanium alloys, Nature 576 (2019) 91–95, doi:10.1038/s41586-019-1783-1.
[13] M.J. Bermingham, D. Kent, H. Zhan, D.H. Stjohn, M.S. Dargusch, Controlling the microstructure and properties of wire arc additive manufactured Ti-6Al-4V with trace boron additions, Acta Mater 91 (2015) 289–303, doi:10.1016/j.actamat.2015.03.035.
[14] R. Banerjee, P.C. Collins, A. Genç, H.L. Fraser, Direct laser deposition of in situ Ti-6Al-4V-TiB composites, Mater. Sci. Eng. A. 358 (2003) 343–349, doi:10.1016/S0921-5093(03)00299-5.
[15] P. Barriobero-Vila, J. Gussone, A. Stark, N. Schell, J. Haubrich, G. Requena, Peritectic titanium alloys for 3D printing, Nat. Commun. 9 (2018) 1–9, doi:10.1038/s41467-018-05819-9.
[16] C.J. Todaro, M.A. Easton, D. Qiu, D. Zhang, M.J. Bermingham, E.W. Lui, M. Brandt, D.H. StJohn, M. Qian, Grain structure control during metal 3D printing by high-intensity ultrasound, Nat. Commun. 11 (2020) 1–9, doi:10.1038/s41467-019-13874-z.
[17] C. de Formanoir, S. Michotte, O. Rigo, L. Germain, S. Godet, Electron beam melted Ti–6Al–4V: Microstructure, texture and mechanical behavior of the as-built and heat-treated material, Mater. Sci. Eng. A. 652 (2016) 105–119, doi:10.1016/j.msea.2015.11.052.
[18] J. Bustillos, J. Kim, A. Moridi, Exploiting lack of fusion defects for microstructural engineering in additive manufacturing, Addit. Manuf. 48 (2021) 102399, doi:10.1016/j.addma.2021.102399.
[19] R. Xin, J. Luo, Q. Ma, Effect of Parameters on Internal Crack Healing in 30Cr2Ni4MoV Steel for 600-Ton Ultra-Super Ingots, Metals (Basel) 7 (2017) 149, doi:10.3390/met7040149.
[20] H. Yu, X. Liu, X. Li, A. Godbole, Crack healing in a low-carbon steel under hot plastic deformation, Metall. Mater. Trans. A Phys. Metall. Mater. Sci. 45 (2014) 1001–1009, doi:10.1007/s11661-013-2049-4.
[21] X.G. Zheng, Y.N. Shi, K. Lu, Electro-healing cracks in nickel, Mater. Sci. Eng. A. 561 (2013) 52–59, doi:10.1016/j.msea.2012.10.080.

[22] A.D. Rollett, U.F. Kocks, A review of the stages of work hardening, Dislocations -93, Los Alamos National Lab, 1993, pp. 1–21 https://www.osti.gov/biblio/10170133-review-stages-work-hardening.
[23] A.F. Jankowski, N. Yang, W.Y. Lu, Constitutive structural parameter cb for the work-hardening behavior of laser powder-bed fusion, additively manufactured 316L stainless steel, Mater. Des. Process. Commun. 2 (2020) e135, doi:10.1002/mdp2.135.
[24] A.F. Jankowski, A constitutive structural parameter cb for the work hardening behavior of additively manufactured Ti-6Al-4V, Mater. Des. Process. Commun. 3 (2021) 1–9, doi:10.1002/mdp2.262.
[25] A.F. Jankowski, J.M. Chames, A. Gardea, R. Nishimoto, E.M. Brannigan, The softening factor cbof commercial titanium alloy wires, Int. J. Mater. Res. 110 (2019) 990–999, doi:10.3139/146.111834.
[26] K. Sofinowski, M. Šmíd, I. Kuběna, S. Vivès, N. Casati, S. Godet, H. Van Swygenhoven, In situ characterization of a high work hardening Ti-6Al-4V prepared by electron beam melting, Acta Mater 179 (2019) 224–236, doi:10.1016/j.actamat.2019.08.037.
[27] R. Shi, Z. Nie, Q. Fan, F. Wang, Y. Zhou, X. Liu, Correlation between dislocation-density-based strain hardening and microstructural evolution in dual phase TC6 titanium alloy, Mater. Sci. Eng. A. 715 (2018) 101–107, doi:10.1016/j.msea.2017.12.098.
[28] F.F. Lavrentev, The type of dislocation interaction as the factor determining work hardening, Mater. Sci. Eng. 46 (1980) 191–208, doi:10.1016/0025-5416(80)90175-5.
[29] P. Krakhmalev, G. Fredriksson, I. Yadroitsava, N. Kazantseva, A. Du Plessis, I. Yadroitsev, Deformation Behavior and Microstructure of Ti6Al4V Manufactured by SLM, Phys. Procedia. 83 (2016) 778–788, doi:10.1016/j.phpro.2016.08.080.
[30] C. de Formanoir, A. Brulard, S. Vivès, G. Martin, F. Prima, S. Michotte, E. Rivière, A. Dolimont, S. Godet, A strategy to improve the work-hardening behavior of Ti–6Al–4V parts produced by additive manufacturing, Mater. Res. Lett. 5 (2017) 201–208, doi:10.1080/21663831.2016.1245681.
[31] P. Castany, F. Pettinari-Sturmel, J. Crestou, J. Douin, A. Coujou, Experimental study of dislocation mobility in a Ti–6Al–4V alloy, Acta Mater 55 (2007) 6284–6291, doi:10.1016/j.actamat.2007.07.032.
[32] R. Keller, W. Zielinski, W.W. Gerberich, On the onset of low-energy dislocation substructures in fatigue: Grain size effects, Mater. Sci. Eng. A. 113 (1989) 267–280, doi:10.1016/0921-5093(89)90315-8.
[33] I.S. Kim, J.M. Oh, S.W. Lee, J.-T. Yeom, J.-K. Hong, C.H. Park, T. Lee, Accelerating globularization in additively manufactured Ti-6Al-4V by exploiting martensitic laths, J. Mater. Res. Technol. 12 (2021) 304–315, doi:10.1016/j.jmrt.2021.02.088.
[34] K. Huang, R.E. Logé, A review of dynamic recrystallization phenomena in metallic materials, Mater. Des. 111 (2016) 548–574, doi:10.1016/j.matdes.2016.09.012.
[35] Y. Cao, H. Di, J. Zhang, J. Zhang, T. Ma, R.D.K. Misra, An electron backscattered diffraction study on the dynamic recrystallization behavior of a nickel-chromium alloy (800H) during hot deformation, Mater. Sci. Eng. A. 585 (2013) 71–85, doi:10.1016/j.msea.2013.07.037.
[36] L.T. Hansen, B.E. Jackson, D.T. Fullwood, S.I. Wright, M. De Graef, E.R. Homer, R.H. Wagoner, Influence of Noise-Generating Factors on Cross-Correlation Electron Backscatter Diffraction (EBSD) Measurement of Geometrically Necessary Dislocations (GNDs), Microsc. Microanal. 23 (2017) 460–471, doi:10.1017/S1431927617000204.
[37] P. Lehto, Adaptive domain misorientation approach for the EBSD measurement of deformation induced dislocation sub-structures, Ultramicroscopy 222 (2021) 113203, doi:10.1016/j.ultramic.2021.113203.
[38] O. Muránsky, L. Balogh, M. Tran, C.J. Hamelin, J.S. Park, M.R. Daymond, On the measurement of dislocations and dislocation substructures using EBSD and HRSD techniques, Acta Mater 175 (2019) 297–313, doi:10.1016/j.actamat.2019.05.036.
[39] R. Wu, M. Zaiser, Cell structure formation in a two-dimensional density-based dislocation dynamics model, Mater. Theory. 5 (2021) 1–22, doi:10.1186/s41313-020-00025-x.
[40] D. Kuhlmann-Wilsdorf, Theory of plastic deformation: - properties of low energy dislocation structures, Mater. Sci. Eng. A. 113 (1989) 1–41, doi:10.1016/0921-5093(89)90290-6.
[41] P. Lehto, H. Remes, T. Saukkonen, H. Hänninen, J. Romanoff, Influence of grain size distribution on the Hall–Petch relationship of welded structural steel, Mater. Sci. Eng. A. 592 (2014) 28–39, doi:10.1016/j.msea.2013.10.094.
[42] J. Zhao, X. Pan, J. Li, Z. Huang, Q. Kan, G. Kang, L. Zhou, X. Zhang, Laser shock peened Ti-6Al-4 V alloy: Experiments and modeling, Int. J. Mech. Sci. 213 (2022) 106874, doi:10.1016/j.ijmecsci.2021.106874.
[43] Y. Zhu, X. Wu, Perspective on hetero-deformation induced (HDI) hardening and back stress, Mater. Res. Lett. 7 (2019) 393–398, doi:10.1080/21663831.2019.1616331.